

Deep Learning for Operational High-Resolution Nowcasting in Switzerland Using Graph Neural Networks

Ophélie Miralles^{a,b}, Daniele Nerini^b, Jonas Bhend^b, Baudouin Raoult^c, Christoph
Spirig^b

^a *Center for Climate Systems Modeling (C2SM), EHTZ, Zürich*

^b *MeteoSwiss, Zürich*

^c *European Centre for Medium-Range Weather Forecasts (ECMWF), Reading, UK*

arXiv:2509.00017v1 [physics.ao-ph] 16 Aug 2025

[†] *Corresponding author: Ophélie Miralles, ophelia.miralles@usys.ethz.ch*

ABSTRACT

Recent advances in neural weather forecasting have shown significant potential for accurate short-term forecasts. However, adapting such gridded approaches to smaller, topographically complex regions like Switzerland introduces computational challenges, especially when aiming for high spatial (1 km) and temporal (10 minutes) resolution. This paper presents a Graph Neural Network (GNN)-based approach for high-resolution nowcasting in Switzerland using the Anemoi framework and observational inputs. The proposed model combines surface observations with selected past and future numerical weather prediction (NWP) states, enabling an observation-guided interpolation strategy that enhances short-term accuracy while preserving physical consistency. We evaluate the method on multiple surface variables and compare it against operational high-resolution NWP (ICON) and nowcasting (INCA) baselines. The results show that the GNN model consistently outperforms traditional approaches in lead times up to 12 hours, especially for wind and precipitation. A comprehensive verification procedure, including spatial skill scores, event-based evaluation, and blind tests with professional forecasters, demonstrates the operational relevance of the approach for mountainous domains.

1. Introduction

Nowcasting, also referred to as very short-term forecasting, involves rapid correction of the most recently available numerical weather prediction (NWP) model run with real-time observations. Traditional nowcasting systems such as INCA, the MeteoSwiss operational nowcasting system, combine three main approaches (Haiden et al. 2011): Lagrangian extrapolation of analysis fields when available (for example, for cloudiness or precipitation), interpolation of residuals at sparse locations with surface measurements and simple blending with NWP model outputs. The nowcasted variable of interest is typically a weighted sum of these three terms, in which the weight attributed to NWP model output is low for short lead times as persistence of observations is more skillful, and increases with the lead time in order to favour seamlessness. The nowcasting lead time range is typically from zero to six hours with a sub-hourly time granularity corresponding to the observation update rate. The spatial resolution for nowcasting output is equally high, usually on the order of 1km. Operational nowcasting is mostly used for weather-dependent decision-making and is thus based on surface variables. In contrast, NWP forecasts a wide range of variables across multiple pressure levels up to ten days ahead with coarser temporal granularity. Nowcasting requires fully automated, ultra-fast data ingestion and processing to produce reliable outputs in very short lead times (0 to 6 h), often updating every few minutes.

Recent work in machine learning, particularly deep learning, has focused on improving precipitation nowcasting from radar data (Shi et al. 2015, 2017; Agrawal et al. 2019; Leinonen et al. 2021; Ravuri et al. 2021; Zhang et al. 2023), with notable success in capturing extreme (Zhang et al. 2023) or convective (Ravuri et al. 2021) events. Deep learning models offer a fundamental shift from conventional nowcasting approaches by learning the nonlinear development of precipitation fields, rather than relying on simplistic assumptions of persistence and advection. This enables them to anticipate complex spatio-temporal patterns such as rapid intensification and localized extremes. Those characteristics, which cause the greatest damage and socioeconomical impacts

(Ravuri et al. 2021; Zhang et al. 2023), but are typically smoothed out or missed by traditional methods. Importantly, our work highlights that leveraging the joint correlations of surface variables (beyond precipitation alone) can provide richer predictive signals, an aspect that remains underexplored in most existing deep learning models focused only on precipitation.

Observation-driven methods aiming to forecast several surface variables at the same time show encouraging first results on the nowcasting range in the United States of America (Sønderby et al. 2020; Andrychowicz et al. 2023). The MetNet3 approach, for example, combines a U-Net architecture with a visual transformer to assimilate diverse weather data and generate reliable forecasts on large domains (Andrychowicz et al. 2023). Although the contributions of the MetNet team are influential (Sønderby et al. 2020; Andrychowicz et al. 2023), the reproducibility of their models remains challenging due to limited public documentation and implementation details.

Most of the models mentioned above are built for large, relatively flat domains. In topographically complex regions like Switzerland, operational nowcasting faces major challenges, including terrain-modulated wind and temperature fields, sharp spatial gradients, and the need for seamless integration with NWP. Building on recent successful data-driven regional modelling efforts (Price et al. 2024; Lang et al. 2024b,a; Alexe et al. 2024; Nipen et al. 2024), we propose an alternative approach inspired by GraphCast (Lam et al. 2022) to nowcast wind, temperature, precipitation and humidity in Switzerland. Unlike gridded U-Net architectures, Graph neural networks (GNNs) enable more flexible spatial modeling and efficient computation over irregular domains. Their structure is also well suited to integrating diverse data sources with heterogeneous spatial supports, such as radar, stations, and satellite observations, making them a promising framework for future extensions.

In the graph neural network (GNN) described in this paper, atmospheric interactions are modelled as a graph, with each geographical location (such as a grid cell or weather station) represented by a node. The edges between nodes capture the interactions that

illustrate how weather patterns at different locations influence each other. The network processes data through multiple hidden nodes, refining the information at various levels of granularity, before mapping the processed data back to specific locations via the output nodes.

For operational nowcasting, it is crucial that the models are transparent and reproducible. Therefore, the study presented here is mainly based on anemoi, an open-source and well-documented Python framework recently introduced and used operationally by the European Centre for Medium-range Weather Forecast (ECMWF). Anemoi is intended to facilitate the development, integration, and operational inference of deep learning models for real-time weather forecasting. It comprises training dataset preparation, e.g., common tools to create and pre-process training datasets, configurable, command-line-based model training and inference, and a catalog of weather datasets and trained models open to its community and end users.

This study contributes to operational nowcasting by introducing a multi-variable deep learning approach that leverages diverse surface observations. It also addresses the challenges of generalising over complex mountainous terrain and ensuring spatially coherent, robust predictions suitable for real-time decision-making in operational settings. It is organised as follows. Section 2 describes the data used for the experiments of Section 3. The verification procedure is then presented in Section 5, followed by a detailed analysis of the results. The paper concludes with a final section that offers insights and explores future challenges and potential directions.

2. Data

The present study uses different data sources. When this work was conducted, NWP forecasts of interest were available from August 2023 onward only. The amount of data appears sufficient relative to the size of the model compared to the recent literature (Lang et al. 2024b; Nipen et al. 2024). While two years of 10-minute data provide a greater number of data points than fifty years of 6-hour slices, we acknowledge that higher

temporal resolution does not necessarily translate to proportionally more independent information due to strong temporal and spatial correlations inherent in weather data. However, for nowcasting applications, high-frequency observations are essential as they enable the model to capture rapid changes and short-term dynamics that coarser data may overlook, thereby enhancing immediate forecasts. We also recognize that the dataset may not include sufficient variability or extreme events, particularly those occurring outside the training period, which limits the model’s ability to learn these phenomena.

a. Numerical Weather Prediction

We use ICON (the ICOSahedral Non-hydrostatic modelling framework originally developed by Deutscher Wetterdienst and MPI, see Zängl et al. (2015)) as the NWP reference. The configuration operates at a spatial resolution of 1km, is updated every 12 hours, and uses ECMWF-IFS as boundary conditions. Although ICON-CH1-EPS is reinitialized every 3 hours and is typically made available to downstream applications such as INCA within 1-2 hours after initialization, in this study we chose a 12-hour update interval. This choice reflects both a conservative assumption regarding the realistic availability of input data within the forecast window and practical considerations during the construction of the anemoi datasets. For the purpose of this analysis, the ICON-CH1 data on its original triangular mesh were reprojected on the Swiss radar 1km grid (EPSG: 2056), see Figure 1. It was also linearly interpolated in time to match the 10-minute nowcasting frequency. A wide range of variables were initially considered, including standard surface variables, such as 2-meter temperature and dew point, 10-meter wind components, and rainfall rate, as well as model-level fields for relative humidity (Q), temperature (T), wind components (U, V), and pressure (P). Model levels range from 1 to 80, 80 being the closest to the surface. More details on ICON model levels and their relation with altitude can be found in Section 3.4 of Reinert et al. (2024). However, only the surface variables were ultimately retained, as the upper-level variables did not demonstrate significant predictive skill for short-term forecasting in this study.

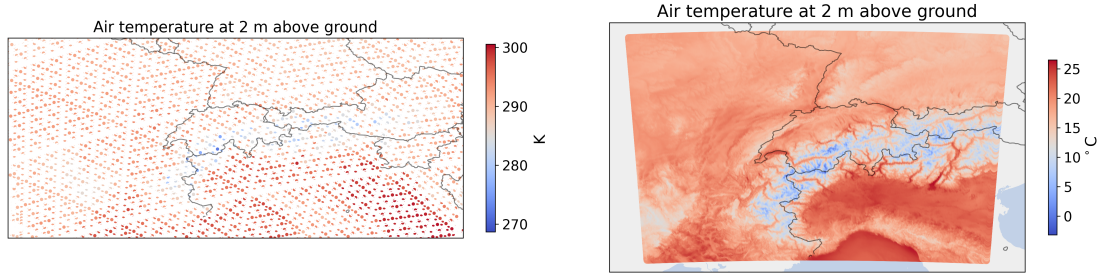


FIG. 1: ICON-CH1-EPS surface temperature data over Switerland on the original triangular mesh (left), rescaled and interpolated to a regular grid (right).

Pre-processing steps, selected variables, date ranges, time frequency and spatial resolution are provided to anemoui-datasets using a YAML configuration file and the command line interface (CLI) provided by the package. The data produced is sorted in a specific order so that slicing it results in 2D fields, and stored in zarr format. An additional wrapper providing a linkage of proprietary data is still necessary for internal sources, although anemoui-datasets provides support for many standard data formats (such as grib or netcdf files). The CLI also enables quick inspection of the build dataset (see Figure 2), whereas opening a zarr file of this size (on the order of terabytes) using standard Python packages like xarray might be very slow or even unfeasible.

b. Observations

Station observations are sourced from the MeteoSwiss Data Warehouse (DWH). Due to the highly variable availability of partner stations over time (as shown on a single date in Figure 3), we selected the 150 SwissMetNet stations with nearly 0% missing values during the training period.

In addition to station data, radar-derived composite data is used for precipitation analysis. The radar product PRECIP (Gabella et al. 2019) provides ground-level precipitation intensity estimates based on a weighted aggregation of reflectivity from all radars above a given pixel. This data is corrected for visibility, reflectivity, and both global and local biases (see Figure 4). Although radar data is collected every five minutes, observations at 10-minute intervals were used to align with the temporal resolution of the station

```

dates:
  start: 2023-08-01T00:00:00Z
  end: 2024-09-09T00:00:00Z
  frequency: 1h
input:
  join:
    - pipe:
      - iconCH1:
          param: [ TOT_PREC, U_10M, V_10M,
                    T_2M, TD_2M, U_75, V_75,
                    T_75, P_75, QV_75, U_80,
                    V_80, T_80, P_80, QV_80 ]
          levtype: sfc
      - interp2res:
          resolution: 1km
          target_crs: epsg:2056
    - dem:
          match_all_dates: true
          param: [ nasadem ]
    - forcings:
          template: ${input.join.0.pipe.1}
          param:
            - cos_latitude
            - cos_longitude
            - sin_latitude
            - sin_longitude
            - insolation
            - cos_local_time
            - sin_local_time
build:
  group_by: daily
  variable_naming: param

```

```

Start      : 2023-08-01 00:00
End        : 2024-09-09 00:00
Frequency  : 1h
Missing    : 0
Resolution : [1.0, 1.0]
Field shape: [1414, 955]

```

```

Shape      : 9,721 x 23 x 1 x 1,350,370 (1.1 TiB)
Size       : 491.8 GiB (491.8 GiB)
Files      : 9,795

```

Index	Variable	Min	Max	Mean	Stddev
0	P_75	56195.8	101848	94095.2	5498.56
1	P_80	56975.5	104435	96357.9	5778.63
2	QV_75	2.84053e-08	0.023279	0.00649169	0.00263497
3	QV_80	9.79577e-07	0.0232343	0.00695471	0.00286014
4	TD_2M	222.454	300.936	280.282	6.59918
5	TOT_PREC	-3.55271e-15	514.266	0.173973	1.44366
6	T_2M	244.781	317.708	284.61	7.40736
7	T_75	244.197	312.909	284.219	7.33054
8	T_80	244.677	315.641	284.754	7.39641
9	U_10M	-32.9181	55.2298	0.747779	2.82935
10	U_75	-50.7867	61.2199	1.80457	5.16394
11	U_80	-33.1365	55.1452	0.744696	2.82217
12	V_10M	-63.9545	47.0865	0.363941	2.79963
13	V_75	-68.6367	56.5952	0.843401	5.02267
14	V_80	-63.8529	47.109	0.361176	2.79245
15	cos_latitude	0.630258	0.743263	0.687468	0.0313377
16	cos_local_time	-1	1	0	0.707107
17	cos_longitude	0.952572	1	0.986632	0.01307
18	insolation	0	0.947992	0.206105	0.272989
19	nasadem	-29	4678	457.108	544.415
20	sin_latitude	0.668999	0.776386	0.724929	0.0297262
21	sin_local_time	-1	1	0	0.707107
22	sin_longitude	-0.0387652	0.304315	0.133875	0.0920019

```

Dataset ready, last update 2 months ago.
Statistics ready.

```

FIG. 2: YAML config used to generate the ICON-CH1-EPS anemoi dataset (left), rendering of the built dataset using the anemoi-datasets CLI (right).

data in this study. The radar composite covers only parts of the Swiss radar domain (Figure 4).

Satellite raw infrared and visible channels are also used as input to the network (see Figure 4 for an example channel). We chose to use the channels presented in Table 1. The Meteosat Second Generation (MSG) system consists of two geostationary satellites positioned at 0°E and 9.5°E. These satellites provide images with a spatial resolution of approximately 3 km (east-west) by 5 km (north-south). Every 15 minutes, a full disk scan captures an image of the entire Earth, while a rapid scan focuses on the upper third of the Earth every five minutes. The satellites alternate their roles, with one conducting the full disk scan while the other performs the rapid scan. The archive retains the data at

Channel	Specificity
IR_108	Has good surface penetration under clear skies. Useful for surface temperature and indirect wind cues.
IR_016	Sensitive to low clouds, aerosols, and snow/ice. Useful for surface analysis, especially during the day. Helps estimate dewpoint indirectly by identifying surface moisture signatures.
VIS006 and HRV	Detect clouds, fog, and surface features. Good for observing low-level cloud movement, which helps infer surface wind and humidity distribution.
IR_039	Useful for fog and low cloud at night, can help indirectly.

TABLE 1: Selected satellite channels and their primary specificities relevant for short-term forecast of surface variables.

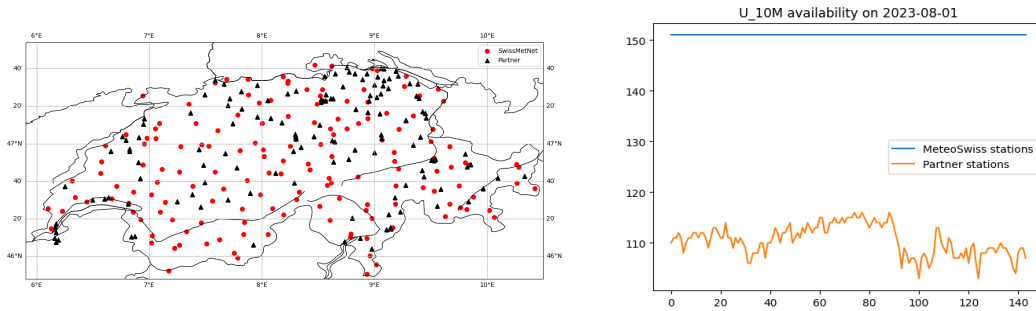


FIG. 3: Left: all available weather stations from SwissMetNet (red bullets) and partner (black triangles) stations. Number of MeteoSwiss/partner stations available per period of 10 minutes on Aug 1 2023 (right).

the highest available resolution, ensuring maximum detail and precision for subsequent analysis. To ensure consistency with the domain and 1km resolution of the radar and nowcasting data, the satellite data is cropped to the Swiss radar grid, interpolated accordingly, and resampled to a 10-minute temporal granularity.

c. Topography

Switzerland’s terrain is complex: local topographic characteristics strongly modify surface wind speeds and temperatures, and to allow the network to learn these relationships, we use the topography of the freely available 90-meter resolution SRTM3

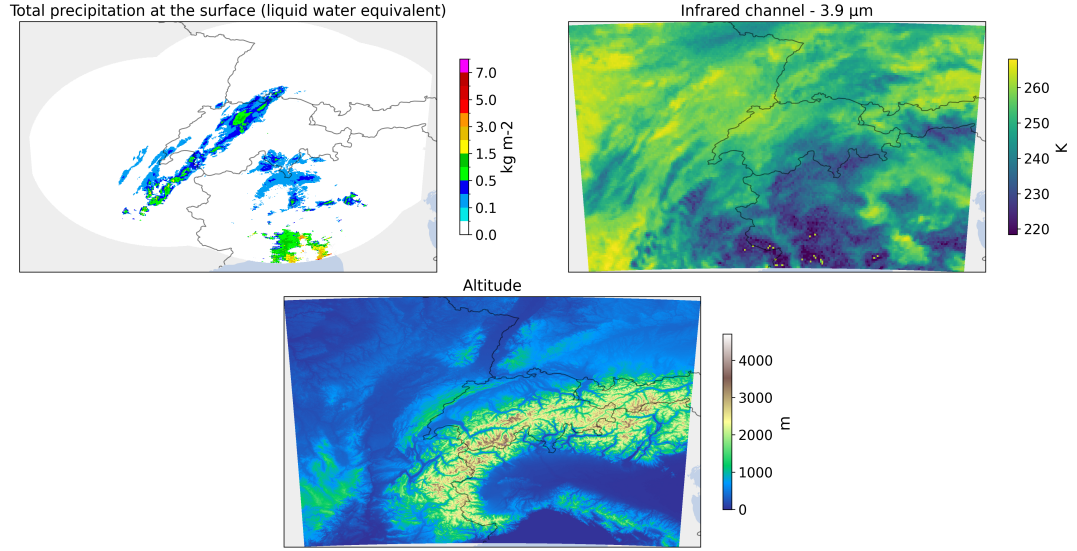


FIG. 4: Composite and raster data: rain rate from radar (top left), infrared channel from MSG satellite (top right), topography (bottom).

digital elevation model (DEM) constructed by NASA and NGA (Jarvis et al. 2008), see Figure 4. Like with satellite data, topography is cropped to the Swiss radar grid and interpolated accordingly.

d. Nowcasting

The Meteoswiss nowcasting system INCA updates every 5-10 minutes, providing continuous forecasts at 1km resolution over the Swiss radar domain. INCA seamlessly combines observed, extrapolated and predicted data from the deterministic ICON run. The current deterministic system runs a single ensemble member. In this study, nowcasting analysis data for 10-meter wind, 2-meter dewpoint, temperature, and rain rate (Sideris et al. 2020) serve as the “ground truth.” The loss of AINCA (Section 3) is calculated against INCA analysis. An analysis, in this context, refers to a high-resolution, observation-informed estimate of the current state of the atmosphere at a specific time (t_0), serving as a reference for evaluating short-term forecasts. Nowcasting forecast data, available every 10 minutes for precipitation and hourly for other surface variables, is also used as a baseline model.

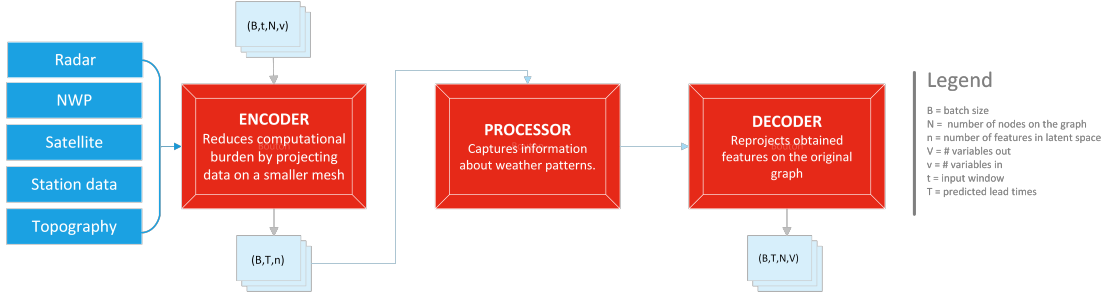
3. General architecture

Below we use the term ‘tensor’ to refer to data provided as input to a neural network, data resulting from the transformation associated with a hidden layer of the network, or predictions made by the network. The network is fed with frames covering the entire domain of interest; in contrast with the use of random square patches (see, e.g., Miralles et al. 2022), the model might be able to learn the domain topography from weather variables and it might alter out-of-sample performance or challenge the understanding of the physical aspects learned by the model. However, training with square patches can result in difficulties reconstituting the full domain for verification and the use of arbitrary smoothing methods on the borders of the patches. We therefore favoured spatial seamlessness for this study, although it might be trickier to apply the model to other regions. To ensure stability and speed of training, we do not update the parameters for each observation but process a ‘batch’ of observations at a time. In this study, all tensors are of dimension four: the first dimension is the batch size, the second is the time coordinate, the third is the flattened spatial coordinate, and the last refers to the “channels”, i.e. individual meteorological variables.

a. Model

Input data on the original data mesh is first encoded into a weather message through attention layers and projected onto a smaller set of nodes, called the hidden mesh, where weather messages are aggregated. Processing then takes place in the smaller set of nodes, to limit the computational burden. Aggregated weather messages are exchanged throughout neighbouring nodes along the edges, thus accounting for spatial correlation. The resulting graph, which contains information on location specificities through the nodes and spatial correlation through the edges, is finally decoded and projected back to the original grid. This model architecture has been extensively described in the recent literature on weather forecasting using graph neural networks (Lam et al. 2022; Lang et al. 2024b,a; Alexe et al. 2024), so is not further detailed here. The main distinction

FIG. 5: Architecture of the model.



from existing medium-range forecasting studies using GNNs lies in the higher temporal resolution, emphasis on surface predictors, and the use of a smaller, higher-resolution spatial domain (with overall more nodes on the graph).

b. Loss function

In the context of this study, nowcasting analysis data was available over Switzerland. We start by training an initial model, referred to as AINCA (AI-based version of INCA) throughout this study, which is evaluated using a pointwise loss against the INCA local nowcasting analysis (see Section d) used as a ground truth. However, such analysis data may not be readily accessible in all countries, particularly within the nowcasting time frame. To address this limitation, another model, called \mathcal{L} -AINCA, explores the forecasting capabilities of Graph Neural Networks (GNNs) in the absence of nowcasting analysis data, necessitating the use of a more sophisticated loss function.

The loss function for the model trained on station data should incorporate two key aspects of nowcasting. First, the influence of observations should gradually decrease as the lead time increases, aligning with the numerical weather prediction (NWP) update when it becomes available. Second, the model should capture the physical patterns present in the NWP data while closely matching the exact station data at the observation locations. This requires the use of different metrics to evaluate the distances from NWP and observational data.

(i) *Pointwise loss* The Huber loss offers a compromise between mean squared error (MSE) and mean absolute error (MAE), providing sensitivity to small residuals while being more robust to outliers. This makes it particularly suitable in settings where occasional large errors may otherwise disproportionately influence optimization. We employ a node-weighted version of the Huber loss for pointwise comparison,

$$\mathcal{L}_H(y, \hat{y}) = \frac{1}{P} \sum_{i=1}^P w_i \begin{cases} \frac{1}{2}(y_i - \hat{y}_i)^2, & \text{if } |y_i - \hat{y}_i| \leq \delta, \\ \delta \left(|y_i - \hat{y}_i| - \frac{1}{2}\delta \right), & \text{otherwise,} \end{cases} \quad (1)$$

where w is the weight associated with node i (i.e. its influence region), P is the number of SwissMetNet stations, $\delta = 0.1$ is the threshold at which the loss becomes linear, y is the input vector and \hat{y} its estimate.

(ii) *Spatial loss* We use the logarithmic spectral distance (LSD) to assess whether the generated images preserve the spatial structures observed in the target images. The LSD (Rabiner and Juang 1993) is the logarithmic difference in power spectra between the generated and realised samples. The node-weighted version can be expressed as

$$\mathcal{L}_{LSD}(y, \hat{y}) = \sqrt{\frac{1}{2N} \sum_{i \leq N} w_i \left[10 \log_{10} \left(\frac{|f(y_i)|^2}{|f(\hat{y}_i)|^2} \right) \right]^2},$$

where f is the Fourier transform and $|f(\cdot)|^2$ the power spectrum. In Yan et al. (2024), using a probabilistically weighted combination of LSD and Fourier correlation loss (FCL) yields promising results. The FCL is expressed as

$$\mathcal{L}_{FCL}(y, \hat{y}) = 1 - \frac{\text{Re} \left[\sum f(\hat{y}_i) \bar{f}(y_i) \right]}{\sqrt{\sum |f(\hat{y}_i)|^2 \sum |f(y_i)|^2}},$$

where \bar{f} denotes the complex conjugate of f . We then define the spatial loss as

$$\mathcal{L}_S(\hat{y}, y) = \mathbf{1}_{w \leq 0.5} \mathcal{L}_{LSD}(\hat{y}, y) + \mathbf{1}_{w > 0.5} \mathcal{L}_{FCL}(\hat{y}, y),$$

with w sampled uniformly between 0 and 1.

(iii) *Total loss* The final loss for the predicted lead time t is

$$\mathcal{L}(t) = w_1 e^{-\alpha(1-t)} \mathcal{L}_S(y_{\text{NWP}}, \hat{y}) + w_2 e^{-\alpha t} \mathcal{L}_S(y_{\text{radar}}, \hat{y}) + w_3 e^{-\alpha t} \mathcal{L}_H(y_{\text{station}}, \hat{y}), \quad (2)$$

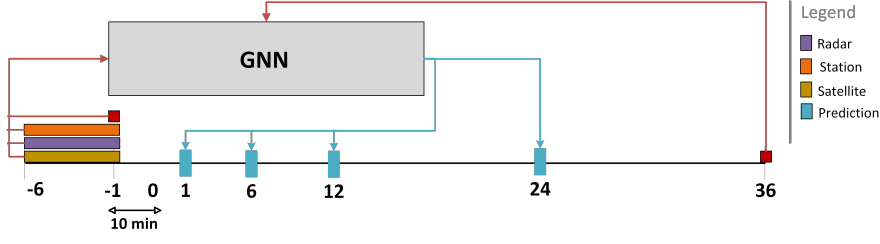
where α is the lead time decay factor. Close to the present time (i.e., t is small), the predictions should be close to the observed values, but when t is large, more importance is given to the loss comparing the predictions to the NWP values. The decay factor and weights were set to $\alpha = 0.15$, $w_1 = 0.4$, $w_2 = 0.4$ and $w_3 = 0.2$ after a qualitative calibration of the hyperparameters, where different weight combinations were manually evaluated by inspecting the model outputs for the validation set (similar to a model validation phase) to identify a configuration that yielded the best results.

4. Seamless interpolation

The model architecture and input data are always the same throughout the study. Predicted surface variables include hourly precipitation in millimeters, 2-meter dew point temperature and temperature in degrees Celsius and 10-meter northward, eastward wind components in meters per second.

The model uses station, satellite and radar observations as well as NWP inputs to predict surface variables of interest. This approach incorporates both past and future NWP states as input to the GNN, allowing it to perform an observation-guided interpolation between these states (see Figure 6). We use one hour of past observations, i.e., six ten-minute windows, and only one past and one future NWP state. The GNN has about 110 M parameters and is trained for 35 epochs on 16 nodes with four GPUs each. Parallel data loading is implemented directly through Anemoi. Convergence is carefully monitored; the validation loss appears to plateau after about 35 epochs.

FIG. 6: Schematic representation of the nowcasting model.



Inference is performed to generate full 12-hour sequences, with a temporal resolution of 10 minutes. Each 12-hour sequence takes approximately 25 seconds to compute, which corresponds to roughly 0.35 seconds per 10-minute timestep on a single GPU.

5. Verification

a. Quantitative: Scores against analysis

Scores are calculated in the test set, which spans the last few months of 2024 (October-December, representing 25% of the training set size). Some scores vary a lot with pointwise discrepancies (e.g., the root mean squared error), whereas some others are designed to focus on spatial patterns (e.g., the fraction skill score). Figure 8 shows both types of scores for models resulting from AINCA and \mathcal{L} -AINCA (see Section 3), evaluated against INCA analysis data, which is considered the ground truth and, as such, is referred to as ‘target’ in some of the plots. Scores for the ICON (red) and INCA (yellow) forecasts are also shown for comparison. The rain rate was not directly available from the ICON forecast output, but was derived by computing the difference in total accumulated precipitation between two consecutive lead times.

Figure 8 yields several insights. The advantage of a nowcasting model is obvious when comparing the ICON and INCA RMSE, quantile scores, and fraction skill score in short lead times for most variables, except for precipitation. In the case of precipitation rate, standard pointwise error metrics, such as RMSE and quantile scores, are less informative due to the so-called *double penalty* effect: small spatial or temporal displacement of

precipitation features can be penalised twice: once for missing the observed location and once for falsely predicting precipitation elsewhere. As a result, only the fraction skill score (here computed over 3km patches), which accounts for spatial tolerance, clearly indicates that INCA outperforms ICON for rain rate. AINCA (dark blue) was trained to emulate INCA analysis. Interestingly, the model prioritises temporal consistency over achieving a perfect score at time zero, which could be related to the value of the hyperparameter α , which controls the rate at which observations lose relevance as lead time increases (Section b). INCA forecasts are designed to match the analysis at time zero and blend into ICON forecasts by around +6 hours: we observe a discrepancy in skill that may stem from using different ICON runs than those employed operationally in INCA.

For the rain rate, AINCA and \mathcal{L} -AINCA consistently outperform both the INCA and ICON forecasts. Beyond a lead time of one hour, AINCA systematically exceeds the INCA forecast system for all variables. \mathcal{L} -AINCA consistently outperforms ICON and also exceeds INCA forecast performance for wind components when evaluated using the fraction skill score. Surprisingly, the GNN struggles most with temperature variables, despite these being among the most predictable. As shown in Figure 7, \mathcal{L} -AINCA tends to overestimate winter temperatures, with the largest deviations from the mean daily pattern occurring at the highest elevation stations.

b. Qualitative: Event-based

Scores alone are insufficient to assess the plausibility of the forecasts generated, so we also visualise key variables for selected events, listed in Table 2. Unlike in the quantitative verification, visualisations can also be qualitatively evaluated for events in the training set, because no sign of overfitting was detected in the quantitative verification and many interesting events occurred in the training period.

Meteograms presented in Figure 9 illustrate how AINCA (trained against INCA analysis with loss from Equation 1) produces smoother patterns than \mathcal{L} -AINCA, which was

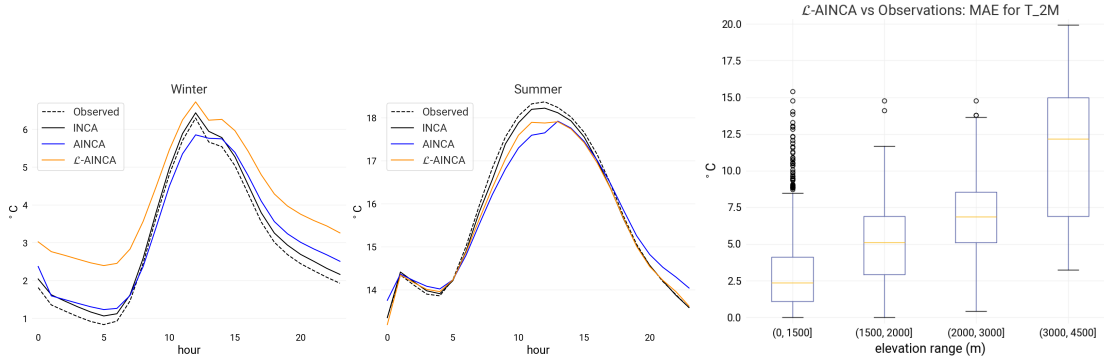


FIG. 7: Spatio-temporal mean daily pattern for predicted air temperature (T_{2M}) in winter and summer compared to analysis (black) and observations (black dotted). Boxplot of the mean absolute error in winter between \mathcal{L} -AINCA predictions and observations, grouped by elevation bins. Note that the bins contain unequal numbers of stations: 1268, 172, 126, and 14 respectively. No significant variation in the T_{2M} MAE distribution is observed for stations located between 0 and 1500 meters elevation.

trained with the loss function \mathcal{L} from Equation 2. During the South Foehn events of February 24 and 25 and March 24, 2024, both AINCA and \mathcal{L} -AINCA models successfully captured key features to be expected at a site in the lee of the mountain range: The foehn onset is characterized by often sharp increases in temperature and wind speed, along with a drop in relative humidity. Altdorf, known for its exposure to Foehn events, serves as a valuable reference point. While the two models are not perfectly aligned, the temporal evolution of the individual variables during Foehn onsets (shortly before noon on 25.2. and morning of 24.3.) is fairly consistent in each of the models and agrees with the physical expectation. Note also differences between the actual observations and the INCA analysis representing a gridded interpolation of observations, the latter being smoother. As shown in Figure 9, the \mathcal{L} -AINCA model tends to produce temporal variations that are more similar to those of the observations than the AINCA model or the analysis data, especially with regards to wind speed.

In addition to event-specific meteograms, time series of maps of variables throughout the day played a key role in model selection for this study. Some models that achieved better quantitative scores exhibited unrealistic spatial patterns, in particular for the rain rate, and were therefore discarded. Instead, hyperparameters were adjusted to priori-

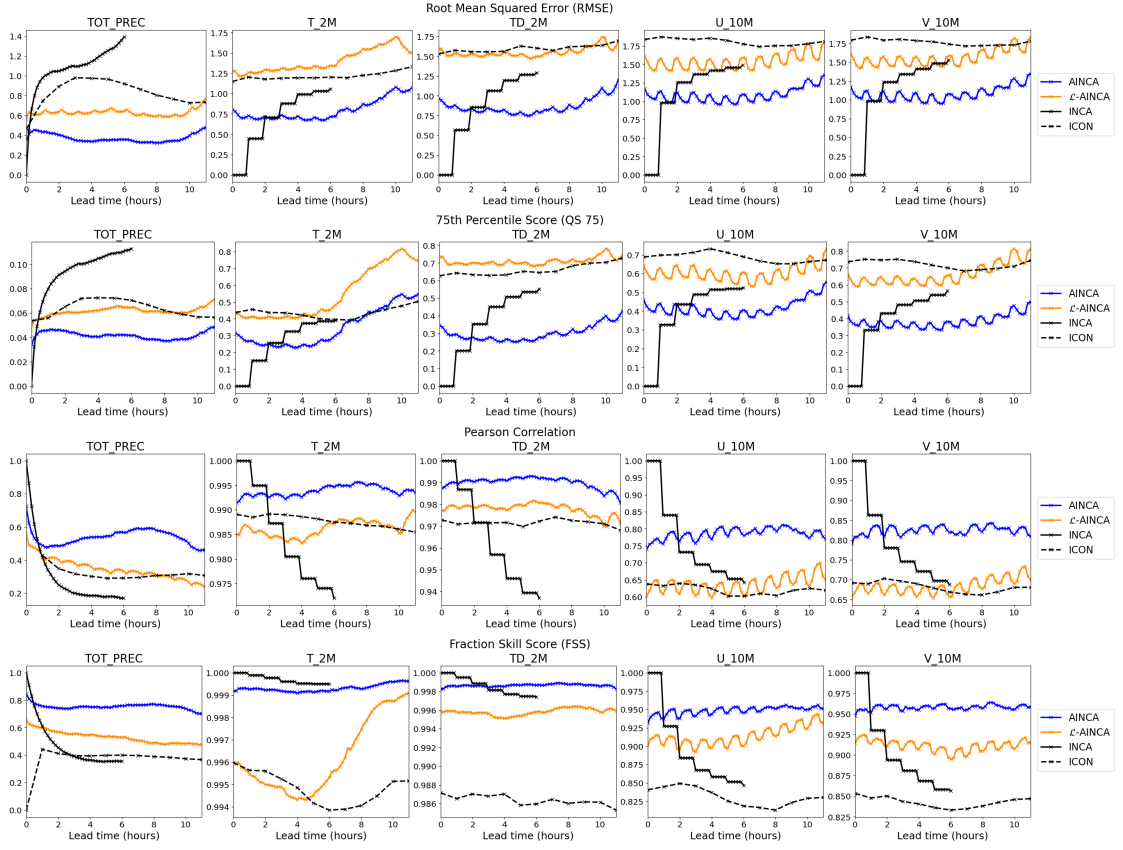


FIG. 8: Root mean squared error (top), Pearson correlation (center), Fraction skill score (bottom). Scores are computed versus INCA analysis; ICON and INCA forecasts are used as baselines for comparison.

tise models that produced more plausible spatiotemporal behaviour. Some illustrative precipitation patterns are shown in Figures 10, and further examples of temperature, dew point, and wind patterns over 12 hours are shown in Figures 11 and 12. Alongside a qualitative evaluation of 12-hourly surface variable patterns, which involved visually inspecting output animations and subjectively selecting configurations that produced the most convincing results, we asked a panel of professional forecasters to identify which outputs were real analyses and which were model predictions. Most of the time, they either found it difficult to tell the difference or made incorrect judgments.

Variable	Start date	End date	Description	Stations
U_10M V_10M	2023-02-25	2023-02-26	Bise situation	KLO, WAE, BER, QUI, SMA, GRA, PAY
U_10M V_10M T_2M	2023-03-12	2023-03-13	Stormy front over Swiss Plateau	CRM, NEU, PAY, MUB, CHA, CHM
U_10M V_10M	2023-03-30	2023-03-31	Storm Mathis	KOP, BER, BAN, GRE, LAG, WYN
U_10M V_10M	2023-06-20	2023-06-21	Dynamic trough leading an active cold front	GVE, CGI, DOL, PRE, BIE
TOT_PREC	2023-08-26	2023-08-29	Hail event in locarno, afterwards heavy precipitation	BIA, LOM
U_10M V_10M	2024-02-24	2024-02-25	South foehn event	ALT, GES, ENG, GLA, CHU
U_10M V_10M	2024-03-01	2024-03-02	South foehn event	ALT, GES, ENG, GLA, CHU
U_10M V_10M	2024-03-08	2024-03-09	South foehn storm	GOR, ZER, SIM, MTE, EVO
U_10M V_10M	2024-03-24	2024-03-26	South foehn event	ALT, GES, ENG, GLA, CHU
U_10M V_10M	2024-06-21	2024-06-22	North foehn combined with thunderstorm outflow	PIO, BIA, CEV, COM, MAG, OTL, LUG
U_10M V_10M TOT_PREC	2024-06-28	2024-06-29	Intense thunderstorms cause flooding in Valle Maggia	ALT, ULR, SIO, MTR, BIA, LUG
U_10M V_10M	2024-09-10	2024-09-14	North foehn event	PIO, COM, BIA, CEV, GRO, MAG, LUG, SBO

TABLE 2: Meteorological events. Stations are specified by their SwissMetNet short name.

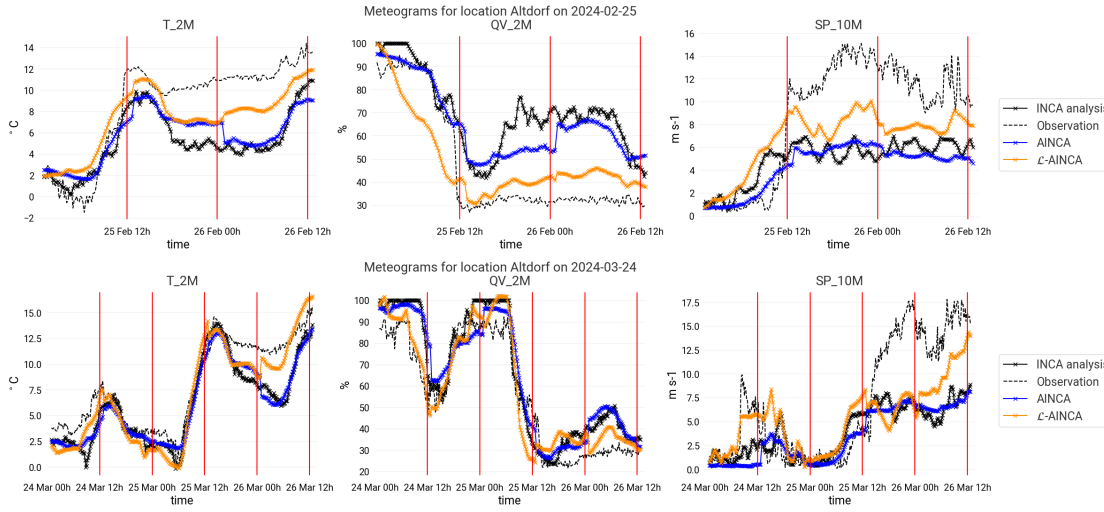


FIG. 9: Meteograms for the 25 February (top) and 24 March (bottom) 2024 South Foehn events at Altdorf (ALT). The first column represents 2-meter temperature, the second relative humidity in % and the last shows the 10-meter wind speed. Events are further described in Table 2. Red vertical lines show successive initialisation times for the AINCA and \mathcal{L} -AINCA forecasts.

6. Conclusion

This study demonstrates the feasibility and advantages of using graph neural networks for high-resolution nowcasting in topographically complex regions such as Switzerland. Using observational data, numerical weather prediction inputs, and a flexible loss function tailored to the nowcasting context, the model can produce forecasts with competitive accuracy and spatial coherence. Furthermore, the inference speed is well within prac-

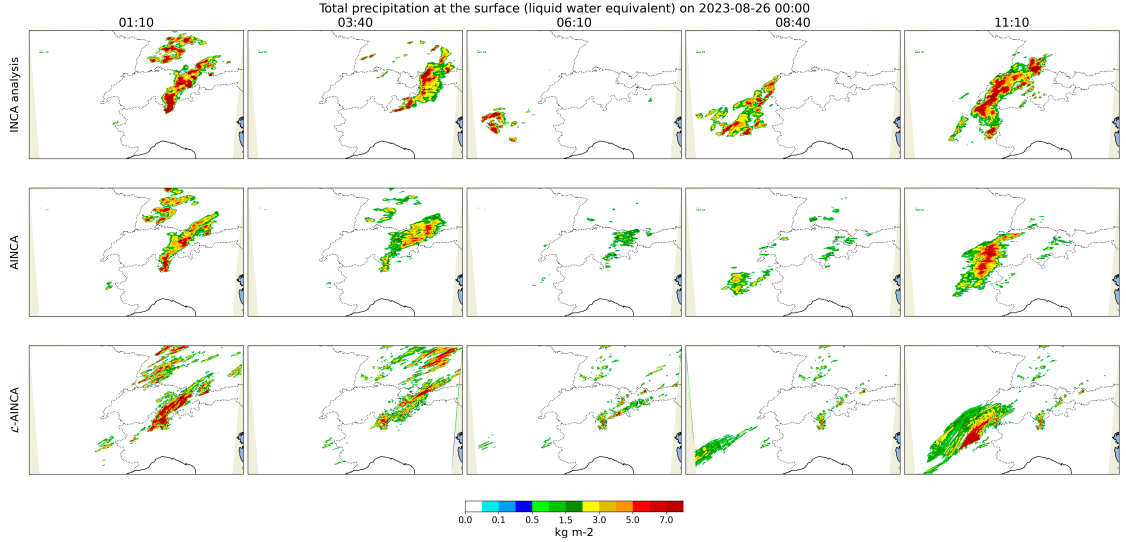


FIG. 10: Example image sequence for instantaneous precipitation (rain rate).

tical limits for deep learning-based forecasting, and significantly faster than traditional numerical models, making it suitable for both research and near-real-time applications.

Quantitative evaluations show that the GNN model outperforms traditional NWP output over the test set (e.g., ICON) and even the operational nowcasting system INCA, particularly beyond the first hour of lead time. Qualitative assessments, both in the form of visual pattern inspections and blind evaluations by professional forecasters, show that the model output is often indistinguishable from real analyses, supporting its operational viability.

A key strength of this work is its integration with the open-source Anemoi framework. By using Anemoi for data preprocessing, training, and inference, the model architecture and pipeline are made transparent and reproducible, facilitating adaptation to other regions or forecasting systems, and suiting the approach for operational deployment and further collaborative development.

Despite these promising results, challenges remain. The temperature variables proved unexpectedly difficult to predict accurately. Additionally, the limited availability of extreme events in the training data may restrict the generalisability of the model in

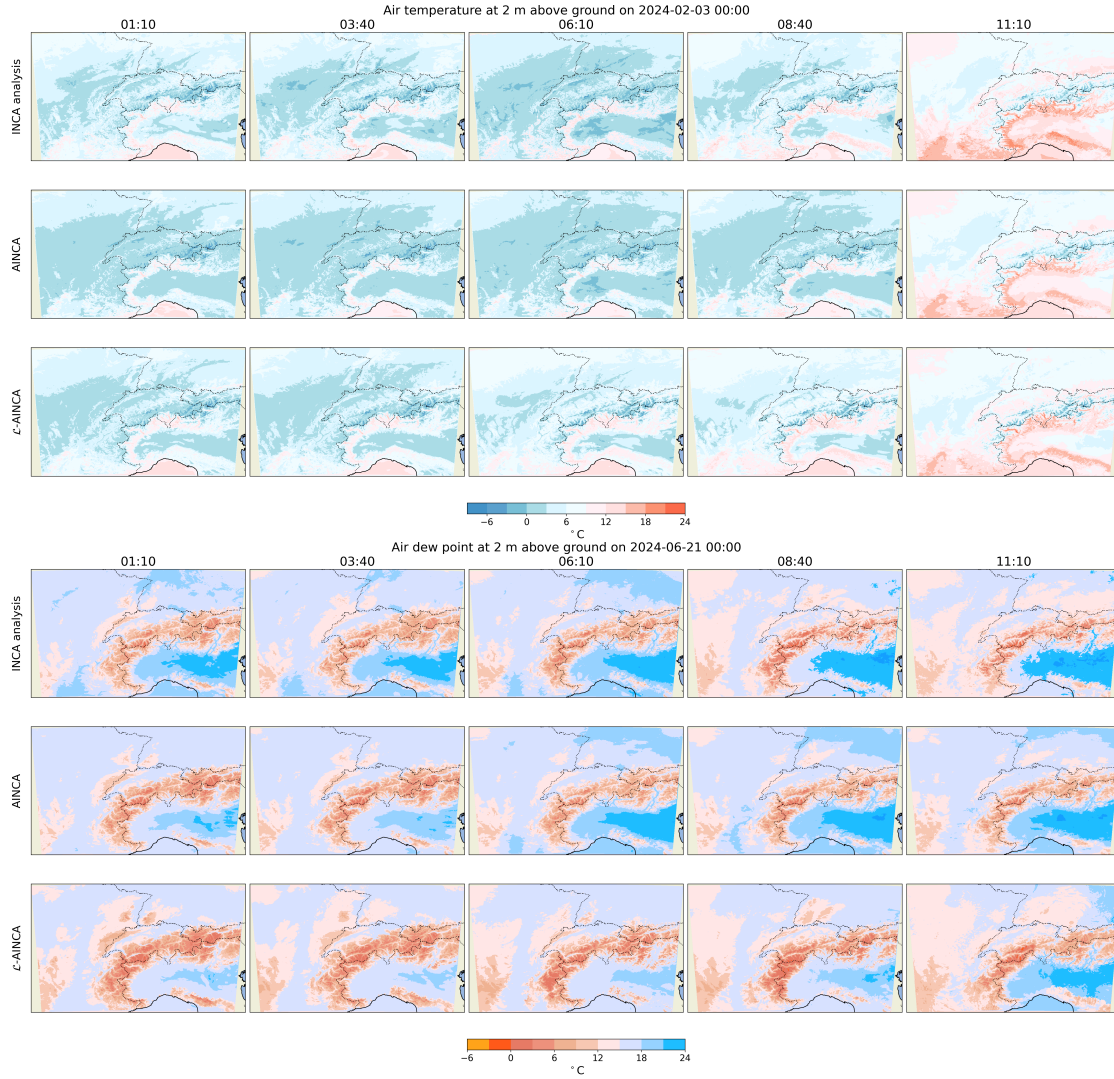


FIG. 11: Example image sequences for 2-meter temperature and 2-meter dew point temperature.

high-impact situations. Furthermore, while the model implicitly handles several types of uncertainty, explicit uncertainty quantification remains an open research direction.

GNN-based nowcasting offers a path forward for localised, high-resolution short-term weather forecasting. Future work should explore the integration of ensemble methods for uncertainty estimation, expanding training datasets to better capture extreme events, and evaluating transferability to other regions.

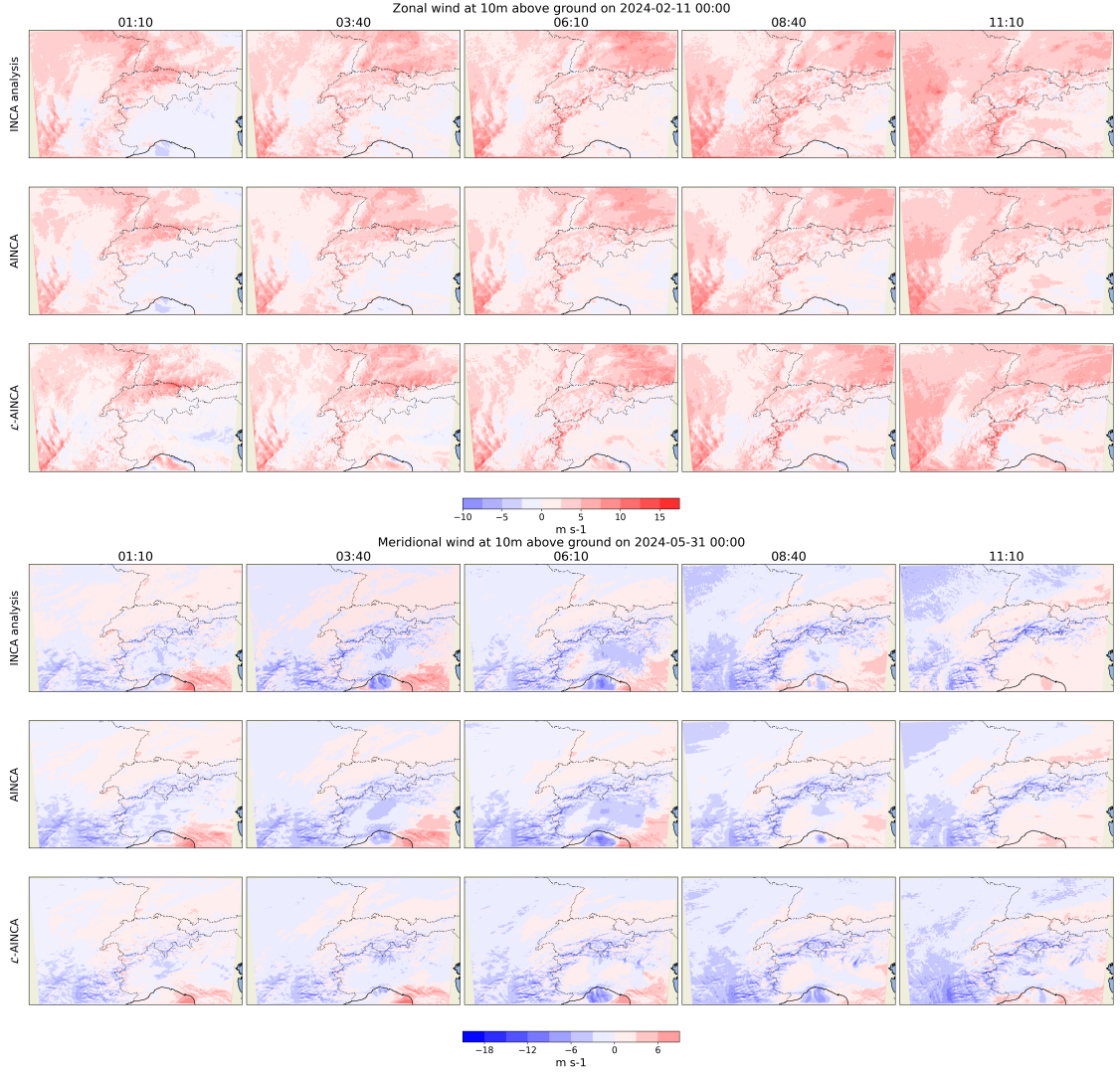


FIG. 12: Example image sequences for 10-meter northern and eastern wind components.

Acknowledgments. Computational resources were provided by the Swiss National Supercomputing Centre (CSCS) and the Federal Office of Meteorology and Climatology (MeteoSwiss), which also provided data. The work benefited from fruitful discussions with the SEPP team at MeteoSwiss and helpful feedback from Anthony Davison (EPFL).

Data availability statement. This study was designed with reproducibility and transferability in mind. The GNN model and training pipeline build on the open source Python package Anemoui and the forks used for this study are available on GitHub

(github.com/OpheliaMiralles/anemoi-training, github.com/OpheliaMiralles/anemoi-models). SwissMetNet station data can be downloaded freely from the MeteoSwiss website (www.meteoswiss.admin.ch/services-and-publications/service/open-data.html), satellite data is available via the EUMETSAT API (data.eumetsat.int), composite radar data can be obtained from the MeteoFrance API (portail-api.meteofrance.fr/web/fr/api/RadarOpera) and topographic data can be downloaded freely from the SRTM 90m DEM Digital Elevation Database (srtm.csi.cgiar.org). Forecast and analysis archive data from the ICON-CH1-EPS and INCA model and from the MeteoSwiss radar are not open-source but can be obtained from MeteoSwiss on demand. Furthermore, MeteoSwiss data is becoming increasingly available as Open Government Data (see opendatadocs.meteoswiss.ch).

Author contribution statement. O.M. conducted the research and wrote the manuscript. B.R. implemented software components critical to nowcasting experiments in anemoi and contributed to technical validation. J.B. provided critical feedback on the manuscript. D.N. contributed to the research direction. C.S. offered suggestions for extending the work. All authors reviewed and approved the final version.

References

- Agrawal, S., L. Barrington, C. Bromberg, J. Burge, C. Gazen, and J. Hickey, 2019: Machine learning for precipitation nowcasting from radar images. *arXiv*, <https://doi.org/10.48550/ARXIV.1912.12132>, URL <https://arxiv.org/abs/1912.12132>.
- Alexe, M., and Coauthors, 2024: GraphDOP: Towards skilful data-driven medium-range weather forecasts learnt and initialised directly from observations. *arXiv*, <https://doi.org/10.48550/ARXIV.2412.15687>, URL <https://arxiv.org/abs/2412.15687>.
- Andrychowicz, M., L. Espeholt, D. Li, S. Merchant, A. Merose, F. Zyda, S. Agrawal, and N. Kalchbrenner, 2023: Deep learning for day forecasts from sparse observations. *arXiv*, URL <http://arxiv.org/abs/2306.06079>, 2306.06079[physics].
- Gabella, M., L. Panziera, I. Sideris, M. Boscacci, D. Wolfensberger, L. Clementi, and U. Germann, 2019: Twelve years of operational real-time hourly precipitation estimation in the Alps: better performance of the radar-only and radar-gauge products in recent years. *Rainfall Monitoring, Modelling and Forecasting in Urban Environment. UrbanRain18: 11th International Workshop on Precipitation in Urban Areas. Conference Proceedings*, N. Peleg, and P. Molnar, Eds., ETH Zurich, Institute of Environmental Engineering, Zurich, 43 – 48, <https://doi.org/10.3929/ethz-b-000347536>, type: Conference Paper.
- Haiden, T., A. Kann, C. Wittmann, G. Pistotnik, B. Bica, and C. Gruber, 2011: The integrated nowcasting through comprehensive analysis (INCA) system and its validation over the eastern alpine region. *Weather and Forecasting*, **26** (2), 166–183, <https://doi.org/10.1175/2010WAF2222451.1>, URL https://journals.ametsoc.org/view/journals/wefo/26/2/2010waf2222451_1.xml.
- Jarvis, A., E. Guevara, H. Reuter, and A. Nelson, 2008: Hole-filled SRTM for the globe: version 4: data grid. CGIAR Consortium for Spatial Information, URL <http://srtm.csi.cgiar.org>, published by CGIAR-CSI on 19 August 2008., <http://srtm.csi.cgiar.org>.

- Lam, R., and Coauthors, 2022: Graphcast: Learning skillful medium-range global weather forecasting. *arXiv preprint arXiv:2212.12794*, <https://doi.org/10.48550/arXiv.2212.12794>, 2212.12794.
- Lang, S., and Coauthors, 2024a: AIFS-CRPS: Ensemble forecasting using a model trained with a loss function based on the continuous ranked probability score. *arXiv*, <https://doi.org/10.48550/ARXIV.2412.15832>, URL <https://arxiv.org/abs/2412.15832>.
- Lang, S., M. Alexe, M. Chantry, J. Dramsch, F. Pinault, B. Raoult, M. Clare, C. Lessig, M. Maier-Gerber, L. Magnusson, and Z. Bouallègue, 2024b: Aifs-ecmwf's data-driven forecasting system. *arXiv preprint arXiv:2406.01465*, 2406.01465.
- Leinonen, J., D. Nerini, and A. Berne, 2021: Stochastic super-resolution for downscaling time-evolving atmospheric fields with a generative adversarial network. *IEEE Transactions on Geoscience and Remote Sensing*, **59** (9), 7211–7223, <https://doi.org/10.1109/tgrs.2020.3032790>.
- Miralles, O., D. Steinfeld, O. Martius, and A. C. Davison, 2022: Downscaling of historical wind fields over Switzerland using generative adversarial networks. *Artificial Intelligence for the Earth Systems*, **1** (4), e220018, <https://doi.org/10.1175/AIES-D-22-0018.1>, URL <https://journals.ametsoc.org/view/journals/aies/1/4/AIES-D-22-0018.1.xml>.
- Nipen, T. N., and Coauthors, 2024: Regional data-driven weather modeling with a global stretched-grid. *arXiv*, <https://doi.org/10.48550/arXiv.2409.02891>, URL <http://arxiv.org/abs/2409.02891>, 2409.02891[physics].
- Price, I., and Coauthors, 2024: GenCast: Diffusion-based ensemble forecasting for medium-range weather. *arXiv*, <https://doi.org/10.48550/arXiv.2312.15796>, URL <http://arxiv.org/abs/2312.15796>, 2312.15796[physics].
- Rabiner, L., and B. Juang, 1993: *Fundamentals of Speech Recognition*. Prentice Hall, Englewood Cliffs, NJ, New Jersey.

- Ravuri, S., and Coauthors, 2021: Skilful precipitation nowcasting using deep generative models of radar. *Nature*, **597 (7878)**, 672–677, <https://doi.org/10.1038/s41586-021-03854-z>, URL <https://www.nature.com/articles/s41586-021-03854-z>.
- Reinert, D., D. Rieger, and F. Prill, 2024: *ICON Tutorial 2024: Working with the ICON Model*. Deutscher Wetterdienst, Business Area “Research and Development”, Frankfurter Straße 135, 63067 Offenbach, URL https://www.dwd.de/DE/leistungen/nwv_icon_tutorial/pdf_einzelbaende/icon_tutorial2024.pdf.
- Shi, X., Z. Chen, H. Wang, D.-Y. Yeung, W.-k. Wong, and W.-c. WOO, 2015: Convolutional LSTM Network: A Machine Learning Approach for Precipitation Nowcasting. *Advances in Neural Information Processing Systems*, C. Cortes, N. Lawrence, D. Lee, M. Sugiyama, and R. Garnett, Eds., Curran Associates, Inc., Vol. 28, URL https://proceedings.neurips.cc/paper_files/paper/2015/file/07563a3fe3bbe7e3ba84431ad9d055af-Paper.pdf.
- Shi, X., Z. Gao, L. Lausen, H. Wang, D.-Y. Yeung, W.-k. Wong, and W.-c. WOO, 2017: Deep Learning for Precipitation Nowcasting: A Benchmark and A New Model. *Advances in Neural Information Processing Systems*, I. Guyon, U. V. Luxburg, S. Bengio, H. Wallach, R. Fergus, S. Vishwanathan, and R. Garnett, Eds., Curran Associates, Inc., Vol. 30, URL https://proceedings.neurips.cc/paper_files/paper/2017/file/a6db4ed04f1621a119799fd3d7545d3d-Paper.pdf.
- Sideris, I. V., L. Foresti, D. Nerini, and U. Germann, 2020: Nowprecip: localized precipitation nowcasting in the complex terrain of switzerland. *Quarterly Journal of the Royal Meteorological Society*, **146 (729)**, 1768–1800, <https://doi.org/https://doi.org/10.1002/qj.3766>, URL <https://rmets.onlinelibrary.wiley.com/doi/abs/10.1002/qj.3766>, <https://rmets.onlinelibrary.wiley.com/doi/pdf/10.1002/qj.3766>.
- Sønderby, C. K., L. Espeholt, J. Heek, M. Dehghani, A. Oliver, T. Salimans, S. Agrawal, J. Hickey, and N. Kalchbrenner, 2020: MetNet: A neural weather model for

precipitation forecasting. *arXiv*, <https://doi.org/10.48550/ARXIV.2003.12140>, URL <https://arxiv.org/abs/2003.12140>.

Yan, C.-W., S. Q. Foo, V. H. Trinh, D.-Y. Yeung, K.-H. Wong, and W.-K. Wong, 2024: Fourier amplitude and correlation loss: Beyond using l2 loss for skillful precipitation nowcasting. *arXiv*, URL <https://arxiv.org/abs/2410.23159>, <https://doi.org/10.48550/ARXIV.2410.23159>.

Zhang, Y., M. Long, K. Chen, L. Xing, R. Jin, M. I. Jordan, and J. Wang, 2023: Skilful nowcasting of extreme precipitation with NowcastNet. *Nature*, **619** (**7970**), 526–532, <https://doi.org/10.1038/s41586-023-06184-4>, URL <https://www.nature.com/articles/s41586-023-06184-4>.

Zängl, G., D. Reinert, P. Rípodas, and M. Baldauf, 2015: The ICON (ICOsahedral non-hydrostatic) modelling framework of DWD and MPI-M: Description of the non-hydrostatic dynamical core. *Quarterly Journal of the Royal Meteorological Society*, **141** (**687**), 563–579, <https://doi.org/10.1002/qj.2378>, URL <https://rmets.onlinelibrary.wiley.com/doi/10.1002/qj.2378>.